Research Article

Mohammed Alrehili*

Synergistic impacts of Thompson–Troian slip, Stefan blowing, and nonuniform heat generation on Casson nanofluid dynamics through a porous medium

https://doi.org/10.1515/ntrev-2025-0230
received June 9, 2025; accepted September 28, 2025

Abstract: A cornerstone of classical fluid dynamics, the no-slip boundary condition posits that fluid particles adjacent to a solid boundary share the velocity of that surface. While this principle is foundational to Navier-Stokes theory, its validity breaks down under certain physical conditions. The present work investigates the hydrodynamic implications of wall slip, characterized by the Thompson–Troian model, on the behavior of a non-Newtonian Casson nanofluid over a stretching surface. In addition, the Stefan blowing effect is incorporated as a key practical consideration. The research also evaluates how variable heat generation interacts with the Cattaneo–Christov heat flux model. The fluid motion in this system is driven by the linear stretching of an elastic sheet embedded in a porous medium, with an applied magnetic field influencing the flow. By applying a suitable mathematical transformation, the governing partial differential equations are converted into ordinary differential equations, which are then solved numerically using the shooting technique. Graphical representations illustrate the behavior of the Casson nanofluid, including velocity profiles, thermal distribution, concentration patterns, and overall flow characteristics. A significant observation from this study is that, compared to the no-slip condition, the presence of slip enhances temperature distribution while reducing nanofluid velocity. The numerical results align well with prior studies, showing strong quantitative agreement. The findings reveal intriguing fluid dynamics phenomena, suggesting potential applications and avenues for future research in this domain.

Keywords: Casson nanofluid, Thompson and Troian slip condition, Stefan blowing, shooting method, Cattaneo–Christov heat flux, nonuniform heat generation

MSC 2020: 202A, 201A

Nomenclature

k_0	permeability of the porous medium (m^2)
a	positive constant (s^{-1})
C	mass concentration of dispersed nanoparticles (mol L^{-1})
u, v	velocity components in x- and y-direction; respectively (m s^{-1})
D_B	Brownian motion coefficient (m^2 s^{-1})
C_w	factor influencing the rate of nanoparticle aggregation on the sheet (mol L^{-1})
M	magnetic parameter
B_0	strength of the imposed magnetic field (T)
B_t	thermophoresis parameter
q'''	volumetric heat generation rate (W m^{-3})
B_r	Brownian motion parameter
f	dimensionless stream representation
Ec	Eckert number
Pr	Prandtl number
u_w	velocity of stretching (m s^{-1})
T_w	heat intensity adjacent to the sheet (K)
c_p	thermal capacity (J kg^{-1} K^{-1})
T	temperature nanofluid (K)
Le	Lewis number
T_∞	thermal level away the sheet (K)
C_∞	factor regulating asymptotic nanoparticle presence (mol L^{-1})

* **Corresponding author: Mohammed Alrehili,** Department of Mechanical Engineering, Faculty of Engineering, University of Tabuk, Tabuk 71491, Saudi Arabia, e-mail: malrehili@ut.edu.sa

Greek symbols

θ	dimensionless temperature
μ	nanofluid viscosity (kg m^{-1} s^{-1})
ϕ	dimensionless concentration
Γ	Casson parameter
Γ_2	temperature coefficient of heat generation
Ω_T	Cattaneo–Christov coefficient (K s^{-2})
κ	thermal conductivity (W m^{-1} K^{-1})
λ_1	hydraulic slip factor (m)
Γ_1	spatial coefficient of heat generation
λ	slip velocity parameter
ρ	density (kg m^{-3})
σ	electric conductivity (S m^{-1})
β	thermal relaxation parameter
δ	porous parameter
ξ	Stefan blowing parameter
ζ	critical shear parameter
ψ	stream function (m^2 s^{-1})
η	similarity variable
ν	kinematic viscosity (m^2 s^{-1})

1 Introduction

Nanofluids represent a class of engineered colloidal suspensions where nanoparticles are uniformly dispersed within a conventional base fluid. These advanced heat transfer media have attracted significant research interest owing to their superior thermal properties and demonstrated potential to substantially improve thermal management efficiency. Consequently, replacing traditional fluids with nanofluids offers considerable advantages in a wide range of cooling and energy systems. Their novel enhanced thermal properties have become a major focus of main applicable researches. Choi [1] pioneered the topic of nanofluids and their researches, and this novel work has spurred considerable interest across different manufacturing and engineering fields. These unique and exceptional properties of nanofluids have prompted many researchers to explore their integration into fundamental manufacturing processes. Further, investigation into nanofluids topics, particularly focusing on heat transfer mechanisms and enhancement through different applicable branches, is a vibrant and active field, especially relevant given the rise of novel technologies and industrial applications. Therefore, nanofluids have include diverse and significant applications across numerous engineering fields, as detailed in the literature [2–8]. These examples, spanning various industries, demonstrate the considerable importance of nanofluids for improving heat and mass transfer mechanism.

Nowadays, within various contemporary industry, optimizing a lot of biomedical processes depends basically on considering slip phenomenon in the flow of fluids that containing nanoparticles. In medical field, especially through designing heart valves, this condition is crucial for accurately managing the flow of blood fluid within it based on the patient's cardiac state. Incorporating nanoparticles within base fluid can present enhanced control to the flow mechanism, leading to decreased friction and enhanced efficiency in artificial heart valve design. Navier [9] was the leader to establish the original study and the cornerstone for the slip phenomenon in fluid mechanics. He also proposed that this phenomenon is basically depends linearly on the shear stress. Based on Navier's foundational work, Maxwell [10] derived a separate relation that can describe gas slip phenomenon at a solid boundary. Because the topic of nanofluids are so important in different applications, it is crucial to use the appropriate model when considering the slip velocity phenomenon. Researches have proved that the Thompson and Troian [11] model is the best and precise model for studying nanofluids when slip velocity is taken into consideration. Numerous studies [12–16] have demonstrated the versatility the significance of Thompson and Troian model in various nanofluid applications and models.

The blowing impact is caused by the movement of some tiny particles, including nanoparticles, from one location to another. This important process plays a crucial role in various physical phenomena such as evaporation, combustion, material synthesis, and distillation. While injection refers to introduce another fluid into a system or base fluid, often under pressure, to control its flow and placement. Stefan blowing [17] describes the mass transfer process or the fluid flow that occurs due to evaporation at a sheet surface. This phenomenon is driven by concentration or temperature gradients, which cause molecules to move either away from or toward the surface. Stefan blowing has a considerable impact on several industrial processes, notably lubrication [18]. Additional noteworthy applications of nanofluids coupled with the Stefan blowing phenomenon are extensively detailed in references [19–21].

This research examines the combined effects of Stefan blowing and the Thompson–Troian slip condition on a Casson nanofluid flowing over a porous stretching sheet, considering variable heat generation and Cattaneo–Christov thermal and mass flux boundary conditions. To the authors' knowledge, no prior study has simultaneously analyzed this comprehensive model, which integrates viscous dissipation, induced magnetism, Ohmic heating, slip mechanisms, blowing effects, and nonuniform thermal generation. By exploring this unique combination of phenomena, the

study addresses a significant gap in the literature and underscores its original contribution to the field.

2 Flow analysis

This study investigates the characteristics of a Casson nanofluid characterized by the Casson parameter Γ in a two-dimensional, steady, and incompressible flow regime, specifically when it is subjected to a stretching sheet. It is well known that Stefan blowing/suction at the sheet can modify the mass transfer rate, leading to changes in the boundary layer thickness and overall heat and mass transfer mechanism. Hence, this serves as a main assumption in this study. Further, the nanofluid velocity flow is assumed to have two components with u representing the x-direction component and v representing the y-direction component (Figure 1).

The stretching process for the elastic sheet occurs through the x-axis, while the y-axis represents the vertical track. A zero net mass flux within the sheet surface is also assumed here, implying an exactly balance between thermophoretic mass flux (caused by temperature gradients) and the mass diffusion (driven by concentration gradients). This balance prevents any net mass transfer through the sheet surface. In addition, the subsequent assumptions are itemized below:

- The model is assumed to impacted by Cattaneo–Christov heat flux model, which is a modified version of Fourier's law of heat conduction.
- Thompson, Troian slip condition is also assumed to impact the model as well as the shear stress at the sheet surface, influencing the overall flow behavior and heat transfer mechanism.
- The model also considers the effect of variable heat generation/absorption, as it affects how effectively heat is transferred.

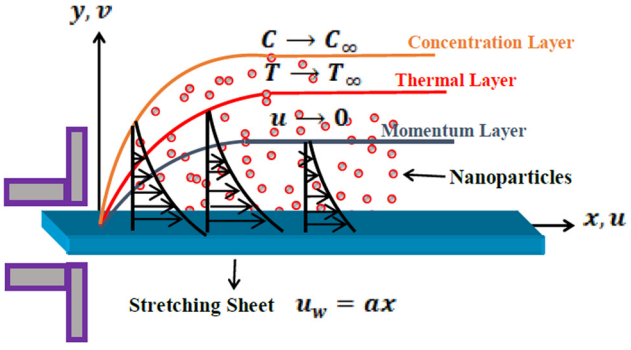

Figure 1: The coordinate flow geometry system.

- Mass flux at the sheet surface also assumed to affect the nanofluid velocity, through the Stefan blowing/suction model.
- Both the concentration C_∞ and temperature T_∞ are considered to be constants and unchanging at a distance away from the sheet's surface.
- The whole model is assumed to be incorporated within a Darcy porous medium.
- The velocity components (u, v) describe the motion of the nanofluid flow through two dimension at any location (x, y) within the boundary region.
- Viscous dissipation is considered in the model, and a magnetic field with a strength of B_0 is employed in the y-direction.

Having outlined the previous model's underlying assumptions, we will now delve into a more detailed investigation of each, including their mathematical representations. We start with a discussion of the Cattaneo–Christov Ω_T phenomenon [22], which can be described as follows [23,24]:

$$\Omega_T = u\left(\frac{\partial u}{\partial x}\frac{\partial T}{\partial x} + \frac{\partial v}{\partial x}\frac{\partial T}{\partial y}\right) + 2uv\frac{\partial^2 T}{\partial x \partial y} + v\left(\frac{\partial v}{\partial y}\frac{\partial T}{\partial y} + v\frac{\partial u}{\partial y}\frac{\partial T}{\partial x}\right) + u^2\frac{\partial^2 T}{\partial x^2} + v^2\frac{\partial^2 T}{\partial y^2}. \tag{1}$$

This phenomenon refines the traditional Fourier law of heat conduction by accounting for a time-relaxation factor. This modification allows for a more realistic description of heat and mass transfer processes that are not instantaneous. A main benefit of this technique is its ability to model and explain heat and mass transfer mechanism under noninstantaneous conditions. Next, we proceed to discuss the details of variable heat generation phenomenon q''' and its mathematical formulation, which takes the following form [25]:

$$q''' = \frac{a\kappa}{\nu}\left[\Gamma_1(T_w - T_\infty)e^{-y\sqrt{\frac{a}{\nu}}} + \Gamma_2(T - T_\infty)\right]. \tag{2}$$

Clearly this relation (2) describes the internal heat generation through the nanofluid motion, which varies with both spatial distribution along the sheet with the coefficient Γ_1 and the temperature gradients with the coefficient Γ_2. Here, ν is the kinematic viscosity, κ is the thermal conductivity and positive values for both Γ_1, Γ_2 means heat generation within the nanofluid flow, while negative values represents heat absorption mechanism. Based on the previously detailed stated assumptions, the following system of equations describe the model for steady, incompressible Casson nanofluid flow [26]:

$$\frac{\partial v}{\partial y} + \frac{\partial u}{\partial x} = 0, \tag{3}$$

$$u\left(\frac{\sigma B_0^2}{\rho}+\frac{\mu}{\rho k_0}\left(1+\frac{1}{\Gamma}\right)\right)+v\frac{\partial u}{\partial y}+u\frac{\partial u}{\partial x}=\nu\left(1+\frac{1}{\Gamma}\right)\frac{\partial^2 u}{\partial y^2}, \tag{4}$$

$$\begin{aligned}&\delta_T\Omega_T+v\frac{\partial T}{\partial y}+u\frac{\partial T}{\partial x}\\&=\frac{\kappa}{\rho c_p}\frac{\partial^2 T}{\partial y^2}+\tau\left[\frac{D_T}{T_\infty}\left(\frac{\partial T}{\partial y}\right)+D_B\frac{\partial C}{\partial y}\right]\frac{\partial T}{\partial y}\\&\quad+\frac{\sigma B_0^2}{\rho c_p}u^2+\frac{q'''}{\rho c_p}+\frac{\nu}{c_p}\left(1+\frac{1}{\Gamma}\right)\left(\frac{\partial u}{\partial y}\right)^2,\end{aligned} \tag{5}$$

$$v\frac{\partial C}{\partial y}+u\frac{\partial C}{\partial x}-D_B\frac{\partial^2 C}{\partial y^2}-\frac{D_T}{T_\infty}\frac{\partial^2 T}{\partial y^2}=0. \tag{6}$$

Now, we begin by defining the physical quantities appearing in the studied model, including the density coefficient, ρ, electric conductivity coefficient σ, permeability of the porous medium k_0, Christov–Cattaneo heat flux coefficient δ_T, thermophoresis diffusion factor D_T, specific heat coefficient c_p, and Brownian motion coefficient D_B. Further, this framework of our model incorporates the synergistic effects of Ohmic heating [27] and viscous dissipation phenomenon [28], acknowledging their substantial impact on modifying the thermal boundary layer structure and augmenting heat transfer processes in electrically conductive fluids. After that, we will describe the boundary conditions, which include a slip velocity that follows the Thompson–Troian slip condition model [29]. This model is highly suitable for studying the flow of nanofluids under various conditions. This model is advantageous due to its nonlinear relationship with shear stress, which provides greater accuracy compared to another simpler models. This feature makes it particularly suitable for nanofluids, where surface forces and molecular interactions are significant. Another important assumption here is the study of the Stefan blowing/suction model [30]. This model, which represent details description for blowing and suction effects, is crucial for understanding mass transfer mechanism during phase change processes such as evaporation and condensation. The following conditions complete our model:

$$\begin{aligned}&u=u_w+\lambda_1\left(\frac{\left(1+\frac{1}{\Gamma}\right)\frac{\partial u}{\partial y}}{\sqrt{1-\zeta_0\left(1+\frac{1}{\Gamma}\right)\frac{\partial u}{\partial y}}}\right),\\&v=\left(\frac{D_B}{C_w-1}\right)\frac{\partial C}{\partial y}\quad\text{at } y=0,\end{aligned} \tag{7}$$

$$T=T_w,\qquad D_B\left(\frac{\partial C}{\partial y}\right)=-\frac{D_T}{T_\infty}\left(\frac{\partial T}{\partial y}\right),\quad\text{at } y=0, \tag{8}$$

$$u\to 0,\quad C\to C_\infty,\quad T\to T_\infty,\quad\text{as } y\to\infty, \tag{9}$$

where ζ_0 is the critical shear rate, $u_w=ax$ is the velocity of the sheet surface, and λ_1 is the coefficient of slip velocity. Moreover, as the critical shear rate vanishes ($\zeta_0=0$), the Thompson–Troian relation converges toward the classical slip formulation, which is better suited for conventional (non-nanofluid) flows. The subsequent step is to define the following dimensionless variables in terms of θ, f, and ϕ as follows [31]:

$$\eta=\left(\frac{a}{\nu}\right)^{\frac{1}{2}}y,\quad \phi(\eta)=\left(\frac{C_\infty-C}{C_\infty-C_w}\right),\quad \theta(\eta)=\left(\frac{T_\infty-T}{T_\infty-T_w}\right). \tag{10}$$

Further, we select the stream function $\psi(x,y)$ with the following definition:

$$\psi=(a\nu)^{\frac{1}{2}}xf(\eta),\quad u=\frac{\partial\psi}{\partial y},\quad v=-\frac{\partial\psi}{\partial x}. \tag{11}$$

Applying dimensionless variables (10) and (11), Eqs. (3)–(6) becomes:

$$\begin{aligned}&\left(1+\frac{1}{\Gamma}\right)\frac{\mathrm{d}^3 f}{\mathrm{d}\eta^3}+f\frac{\mathrm{d}^2 f}{\mathrm{d}\eta^2}\\&\quad=\left[\delta\left(1+\frac{1}{\Gamma}\right)+M\right]\frac{\mathrm{d}f}{\mathrm{d}\eta}+\left(\frac{\mathrm{d}f}{\mathrm{d}\eta}\right)^2,\end{aligned} \tag{12}$$

$$\begin{aligned}&\frac{\mathrm{d}^2\theta}{\mathrm{d}\eta^2}+\mathrm{Pr}\left\{B_r\frac{\mathrm{d}\theta}{\mathrm{d}\eta}\frac{\mathrm{d}\phi}{\mathrm{d}\eta}+B_t\left(\frac{\mathrm{d}\theta}{\mathrm{d}\eta}\right)^2\right\}\\&\quad+\Gamma_1 e^{-\eta}-\mathrm{Pr}\beta\left(f\frac{\mathrm{d}f}{\mathrm{d}\eta}\frac{\mathrm{d}\theta}{\mathrm{d}\eta}+f^2\frac{\mathrm{d}^2\theta}{\mathrm{d}\eta^2}\right)+\mathrm{Pr}f\frac{\mathrm{d}\theta}{\mathrm{d}\eta}\\&\quad+\Gamma_2\theta+\mathrm{Pr}\left\{M\mathrm{Ec}\left(\frac{\mathrm{d}f}{\mathrm{d}\eta}\right)^2+\mathrm{Ec}\left(1+\frac{1}{\Gamma}\right)\left(\frac{\mathrm{d}^2 f}{\mathrm{d}\eta^2}\right)^2\right\}=0,\end{aligned} \tag{13}$$

$$B_r\left(\frac{\mathrm{d}^2\phi}{\mathrm{d}\eta^2}\right)+B_t\left(\frac{\mathrm{d}^2\theta}{\mathrm{d}\eta^2}\right)+B_r\mathrm{LePr}\left(f\frac{\mathrm{d}\phi}{\mathrm{d}\eta}\right)=0, \tag{14}$$

with the following boundary conditions imposed:

$$\begin{aligned}&f=\frac{\xi}{Le}\phi',\quad \theta=1,\quad \phi'=-\frac{B_t}{B_r}\theta',\\&f'=1+\lambda\left(\frac{\left(1+\frac{1}{\Gamma}\right)f''}{\sqrt{1-\zeta\left(1+\frac{1}{\Gamma}\right)f''}}\right)\quad\text{at } \eta=0,\end{aligned} \tag{15}$$

$$f'\to 0,\quad \phi\to 0,\quad \theta\to 0\quad\text{as } \eta\to\infty. \tag{16}$$

At this step, we conclude this section by defining the following nondimensional governing factors as follows:

$$\begin{cases} M = \dfrac{\sigma B_0^2}{\rho a} & \text{Magnetic field parameter,} \\ \delta = \dfrac{\mu}{\rho a k_0} & \text{Porous parameter,} \\ B_r = \dfrac{\tau D_B (C_w - C_\infty)}{\nu} & \text{Brownian motion parameter,} \\ \mathrm{Pr} = \dfrac{\mu c_p}{\kappa} & \text{Prandtl number,} \\ \lambda = \lambda_1 \sqrt{\dfrac{a}{\nu}} & \text{Velocity slip parameter,} \\ \mathrm{Le} = \dfrac{\nu}{D_B} & \text{Lewis number,} \\ B_t = \dfrac{\tau D_T (T_w - T_\infty)}{T_\infty \nu} & \text{Thermophoresis parameter,} \\ \beta = \delta_T a & \text{Thermal relaxation time constant,} \\ \zeta = u_w \sqrt{\dfrac{a}{\nu}}\, \zeta_0 & \text{Critical shear rate,} \\ \xi = \dfrac{C_w - C_\infty}{1 - C_w} & \text{Stefan blowing,} \\ \mathrm{Ec} = \dfrac{u_w}{c_p (T_w - T_\infty)} & \text{Eckert number.} \end{cases}$$

Finally, a thorough analysis of the model requires an investigation into how its key parameters influence heat and mass transfer rates $\mathrm{Re}_x^{-\frac{1}{2}}$ and $\mathrm{Re}_x^{-\frac{1}{2}}$, along with the surface friction coefficient $\mathrm{Cf}_x \mathrm{Re}_x^{\frac{1}{2}}$. These quantities takes the forms:

$$\begin{aligned} \mathrm{Cf}_x \mathrm{Re}_x^{\frac{1}{2}} &= -\left(1 + \frac{1}{\Gamma}\right) f''(0), \\ \mathrm{Sh}_x\, \mathrm{Re}_x^{\frac{-1}{2}} &= -\phi'(0), \quad \mathrm{Nu}_x\, \mathrm{Re}_x^{\frac{-1}{2}} = -\theta'(0). \end{aligned} \tag{17}$$

3 Validation of the method's precision

The shooting approach was employed through creating the numerical findings. In this section, we intend to evaluate these numerical findings through a comparison with the previously presented data at the same condition as clear from Table 1. We compare our results with the findings reported by Akbar *et al.* [32] under some special values for the parameters $\delta = \lambda = \xi = 0$ that convert our model to a Newtonian model. The examination take into consideration the magnetic field parameter M to perform this comparative analysis. Clearly that, the presented numerical results through the tabular form are closely align with the present findings, supporting their reliability and accuracy.

Table 1: Comparison of $-f''(0)$ with special values of M when $\delta = \lambda = \xi = 0$ and $\Gamma \to \infty$

M	Akbar *et al.* [32]	Present work
0.0	1.00000	1.0000000000
0.25	1.11803	1.1180295840
1.0	1.41421	1.4141987402

4 Numerical methodology

For enhanced clarity, Figure 2 presents a schematic overview of the implemented numerical method. This diagram delineates the computational algorithm regarding the shooting method, beginning with the conversion of the governing partial differential equations into a system of ordinary differential equations. Subsequent steps include imposing the relevant boundary conditions, making iterative estimates for missing initial values, performing numerical integration via the Runge–Kutta scheme, and conducting successive verification of convergence until the predefined tolerance is met.

5 Findings and interpretation

In this section, a comprehensive numerical examination, based on the shooting technique, was conducted via a range of factor values that govern the model to clarify the physical problem. The findings data are introduced graphically in Figures 3–11 and presented in Table 2. Figure 3 shows how a dimensionless slip velocity parameter λ affects the flow characteristics including velocity $f'(\eta)$, temperature $\theta(\eta)$, and concentration $\phi(\eta)$. It is noted from the analysis that an increase in the slip parameter λ can significantly reduce the flow velocity $f'(\eta)$, which aligns with the expected physical concept of the surface slip phenomenon. Physically, the slip phenomenon always reduces the friction force that already exist between the sheet surface and the nanofluid, resulting in a reduce for the flow velocity in the near-the sheet surface. Also, the effect of the same factor on temperature $\theta(\eta)$ is evident in Figure 3(c) through the increase behavior in temperature with increasing it, indicating that heat transfer becomes more efficient as the slip factor effect intensifies. In addition, the presence of slip phenomenon clearly affects the distribution of nanoparticles in the boundary layer region. Clearly that, the nanofluid's concentration $\phi(\eta)$ exhibits an observable decline behavior close to the sheet surface,

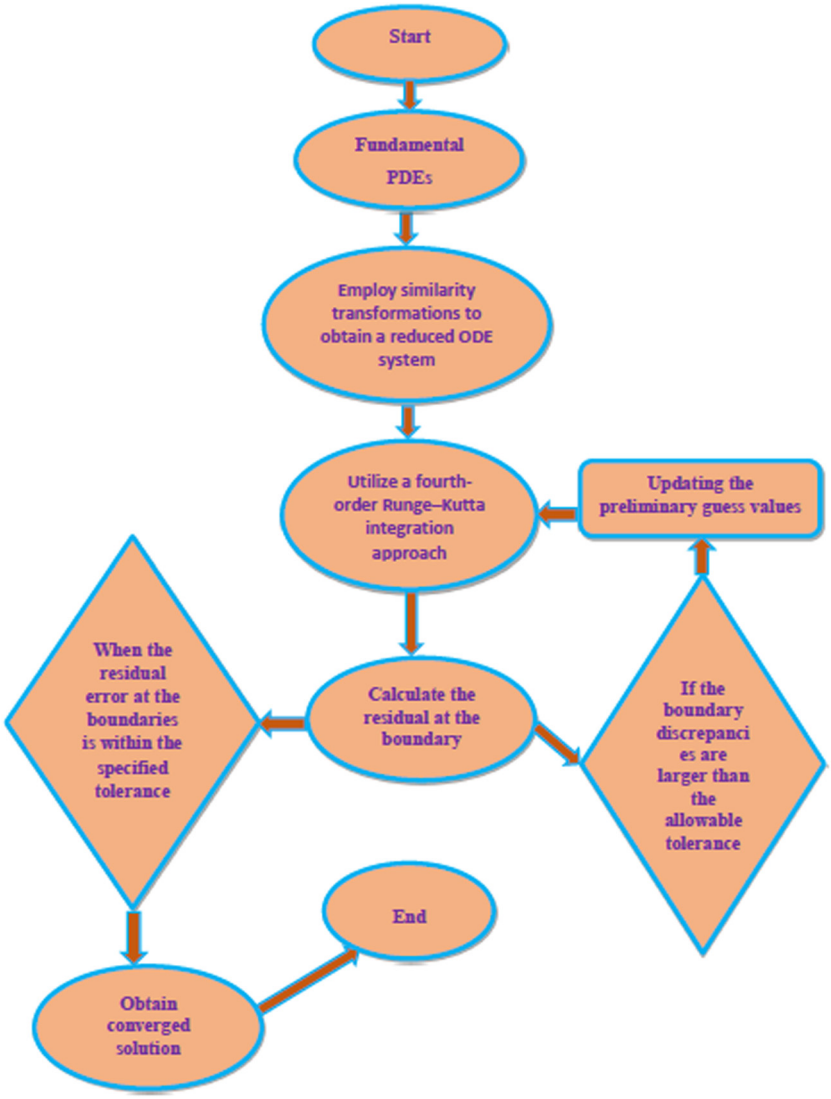

Figure 2: Flowchart of the computational approach.

dipping into negative values. It then steadily enhances before experiencing a sharp reduce, ultimately reaching zero at the ambient.

As a further examination of the Casson nanofluid flow behavior with and without slip velocity parameter ($\lambda = 0.4, \lambda = 0.0$), Figure 4 is presented to further compare the distribution and the shape of streamlines $\psi(x, y)$ in both cases. In spite of it is expected that the slip velocity phenomenon at a surface slows down the overall flow velocity, it simultaneously decreases the restrictive impact of the boundary layer region, allowing the fluid to move more freely and enhancing the density of streamlines.

One of the important phenomena in this study, which cannot be overlooked, is the investigation of the effect of the magnetic field as a function of magnetic number M and how it controls the nanofluid properties through its velocity $f'(\eta)$, temperature $\theta(\eta)$, and concentration $\phi(\eta)$, as illustrated in Figure 5. It is noteworthy that near the surface ($0 \le \eta \le 1.2$) of the elastic sheet, the fluid concentration $\phi(\eta)$ is initially lower than zero $\phi(\eta) < 0$, then rises, passing through a zero concentration point, and continues to rise. Immediately after that, the concentration reduces until it reaches zero at a point farther from the elastic sheet surface. It is also important to note the impact of the magnetic field and its strength on both the velocity and temperature fields of the Casson nanofluid. It is clearly noticeable that the magnetic field acts as a stimulating factor for temperature distribution in an organized manner. Physically, the presence of the magnetic field suppresses the field of nanofluid velocity due to the presence of the Lorentz force, which is responsible for this phenomenon, whether in terms of velocity reduction or enhanced

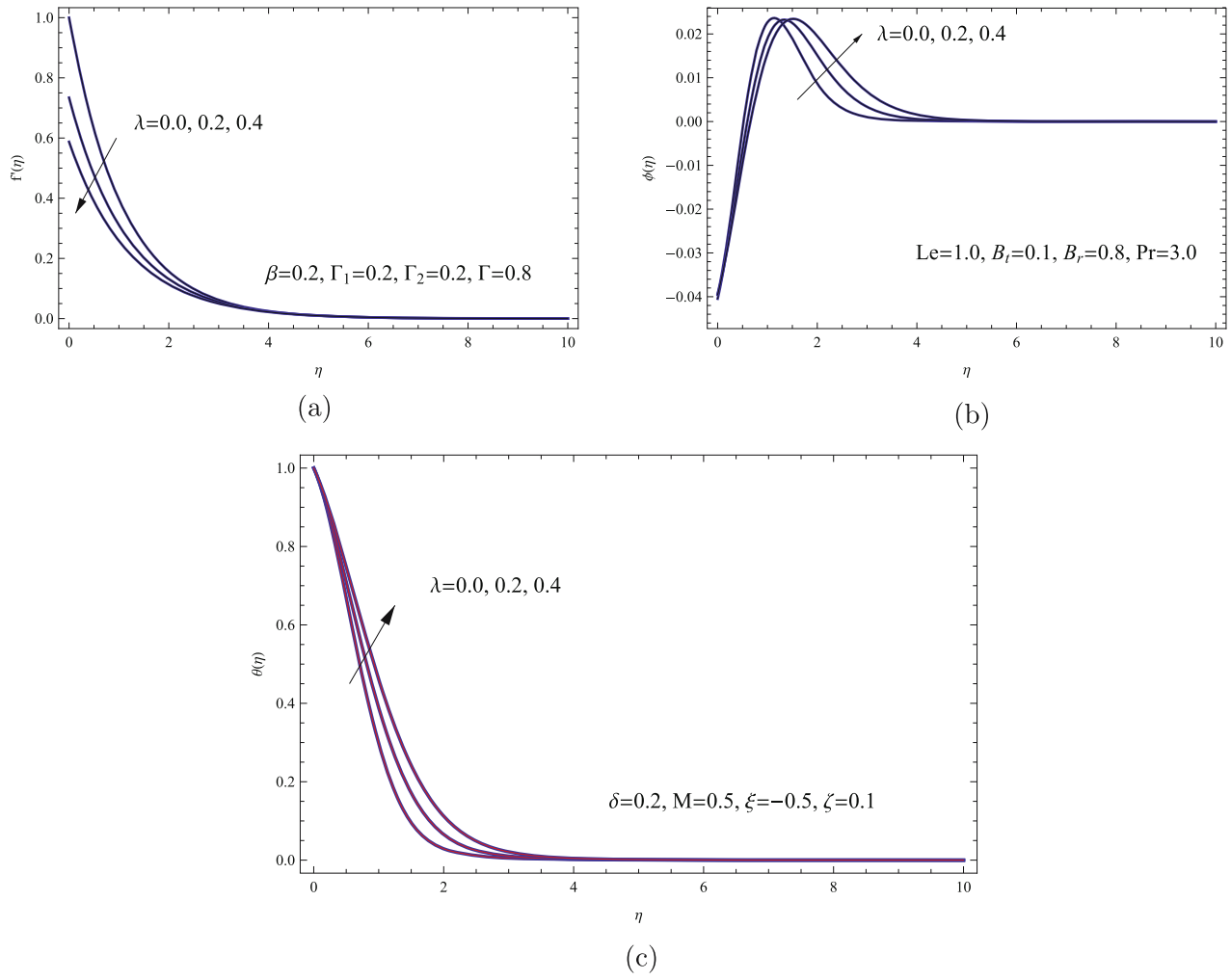

Figure 3: (a) $f'(\eta)$ via varying λ, (b) $\phi(\eta)$ via varying λ, and (c) $\theta(\eta)$ via varying λ.

Table 2: Values of $\mathrm{Sh}_x\mathrm{Re}_x^{\frac{-1}{2}}$, $\mathrm{Cf}_x\sqrt{\mathrm{Re}_x}$, and $\mathrm{Nu}_x\mathrm{Re}_x^{\frac{-1}{2}}$ for different values of the controlling parameters with $\xi = -0.5$, $\mathrm{Le} = 1.0$, $\zeta = 0.1$, $\beta = 0.2$, $\Gamma = 0.8$, and $\mathrm{Pr} = 3.0$

λ	M	δ	Γ_1, Γ_2	B_t	B_r	$\mathrm{Cf}_x\sqrt{\mathrm{Re}_x}$	$\mathrm{Nu}_x\mathrm{Re}_x^{\frac{-1}{2}}$	$\mathrm{Sh}_x\mathrm{Re}_x^{\frac{-1}{2}}$
0.0	0.5	0.2	0.2	0.1	0.8	2.08362	0.351757	0.039327
0.2	0.5	0.2	0.2	0.1	0.8	1.42029	0.390025	0.040457
0.4	0.5	0.2	0.2	0.1	0.8	1.08602	0.356028	0.042554
0.2	0.0	0.2	0.2	0.1	0.8	1.25022	0.549157	0.046585
0.2	0.5	0.2	0.2	0.1	0.8	1.42029	0.390025	0.040457
0.2	1.0	0.2	0.2	0.1	0.8	1.55925	0.263494	0.035459
0.2	0.5	0.0	0.2	0.1	0.8	1.27024	0.462919	0.043889
0.2	0.5	0.5	0.2	0.1	0.8	1.60148	0.295784	0.035694
0.2	0.5	1.0	0.2	0.1	0.8	1.83355	0.164477	0.028593
0.2	0.5	0.5	0.0	0.1	0.8	1.59771	0.546514	0.044552
0.2	0.5	0.5	0.2	0.1	0.8	1.60148	0.295784	0.035694
0.2	0.5	0.5	0.4	0.1	0.8	1.60597	0.002464	0.025868
0.2	0.5	0.5	0.2	0.1	0.8	1.60148	0.295784	0.035694
0.2	0.5	0.5	0.2	0.2	0.8	1.59888	0.234519	0.068613
0.2	0.5	0.5	0.2	0.5	0.8	1.59813	0.103780	0.142317
0.2	0.5	0.5	0.2	0.1	0.5	1.59925	0.277852	0.057671
0.2	0.5	0.5	0.2	0.1	0.8	1.60148	0.295784	0.035694
0.2	0.5	0.5	0.2	0.1	1.5	1.60343	0.311687	0.018883

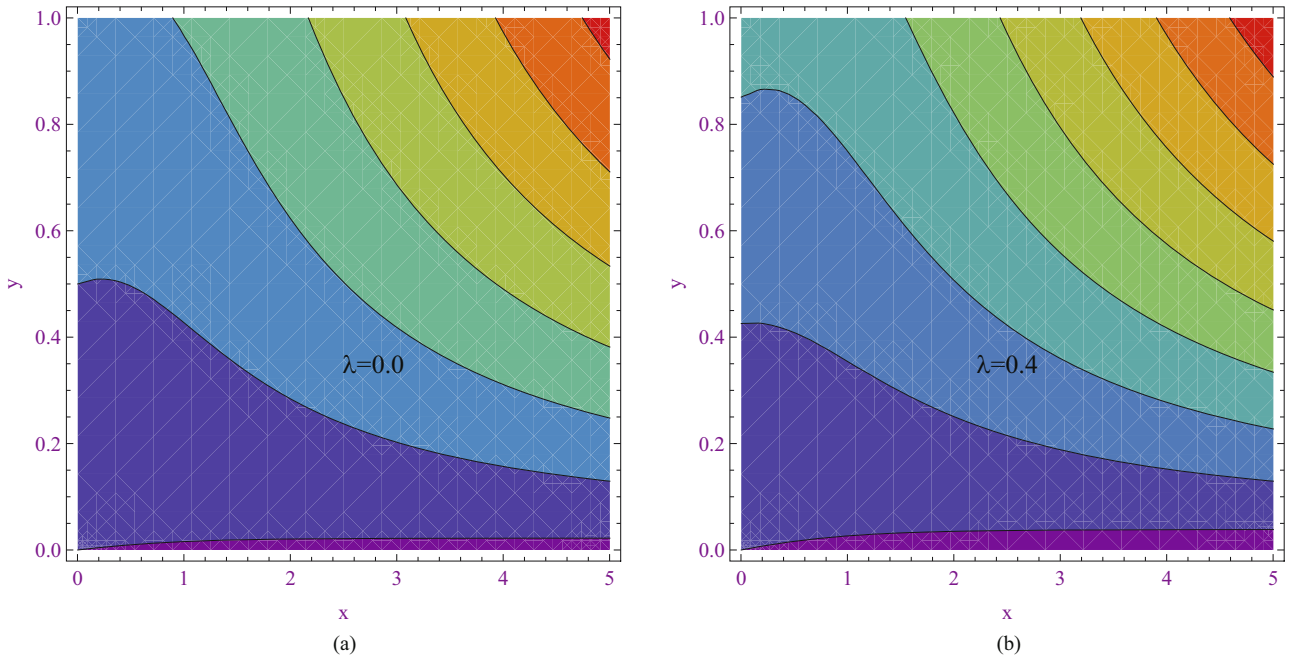

Figure 4: (a) Stream function with λ = 0.0 and (b) stream function with λ = 0.4.

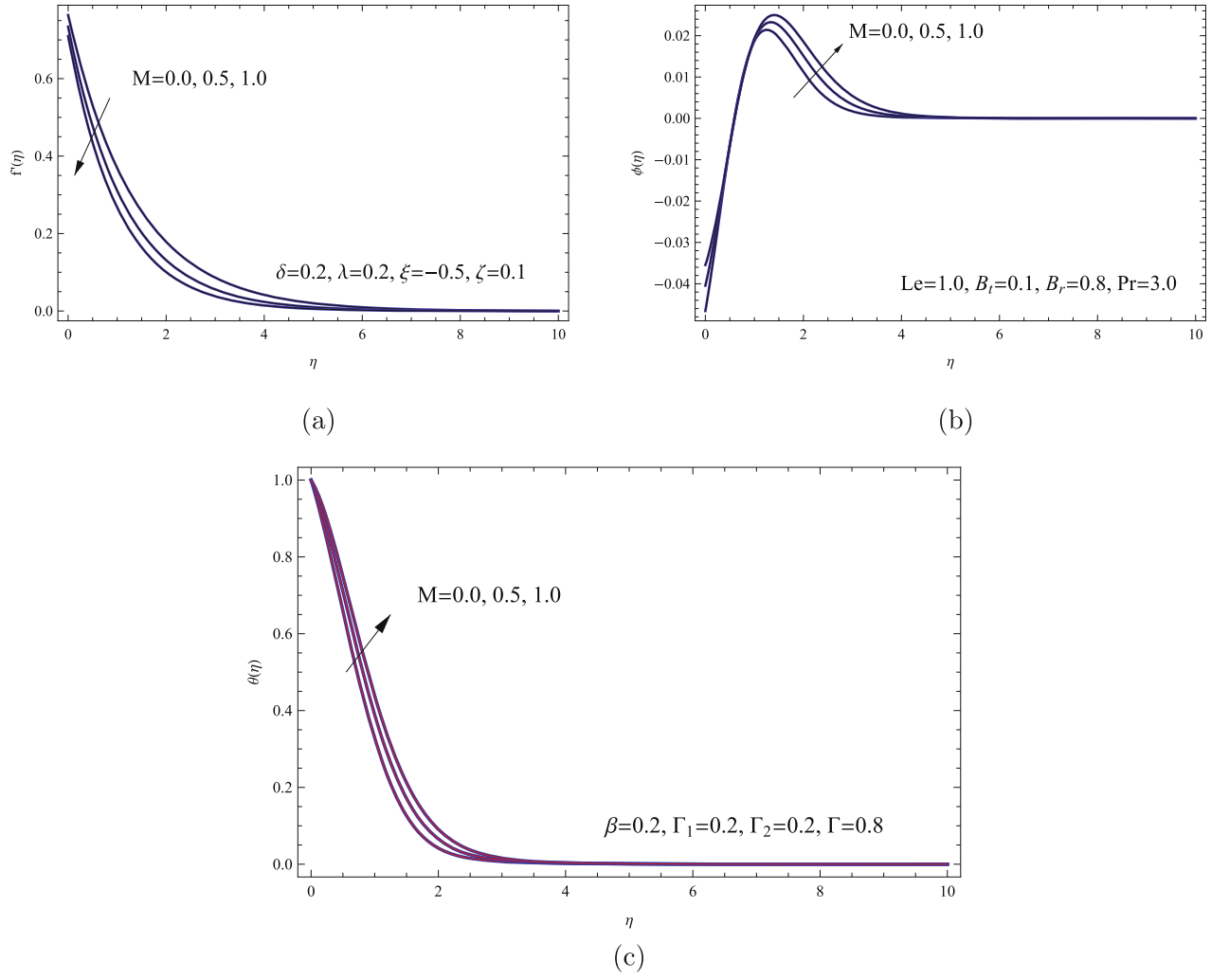

Figure 5: (a) $f'(\eta)$ via varying M and (b) $\phi(\eta)$ via varying M, and (c) $\theta(\eta)$ via varying M.

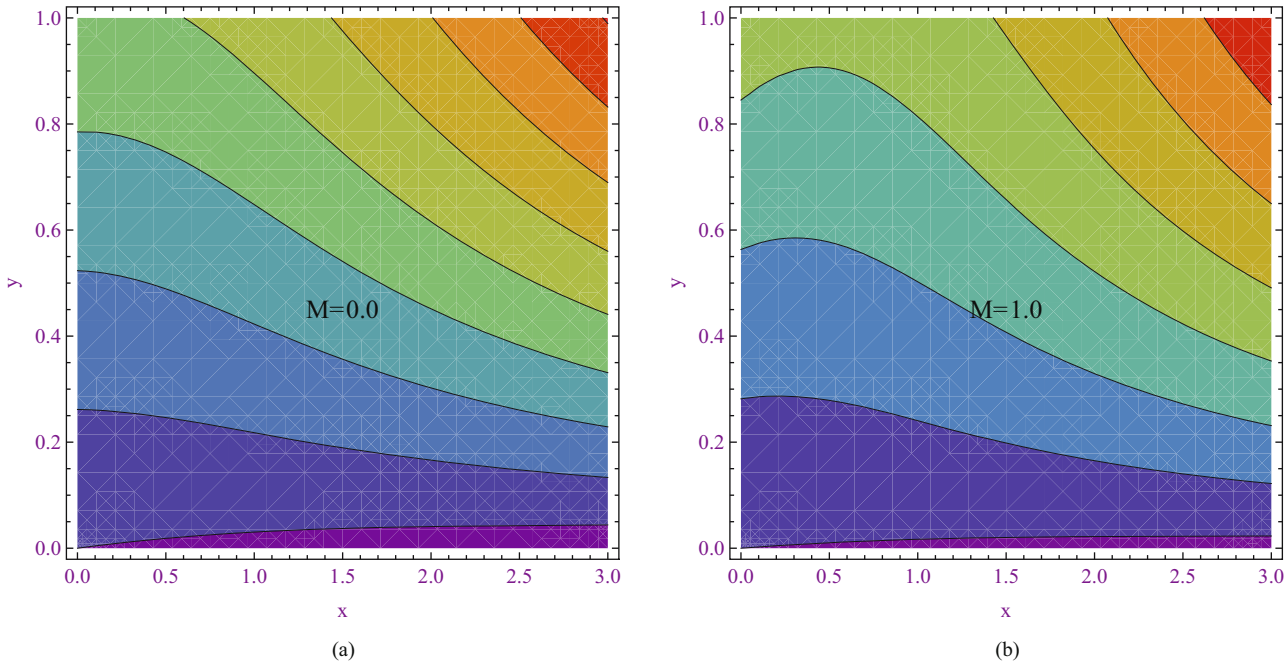

Figure 6: (a) Stream function with M = 0.0 and (b) stream function with M = 1.0.

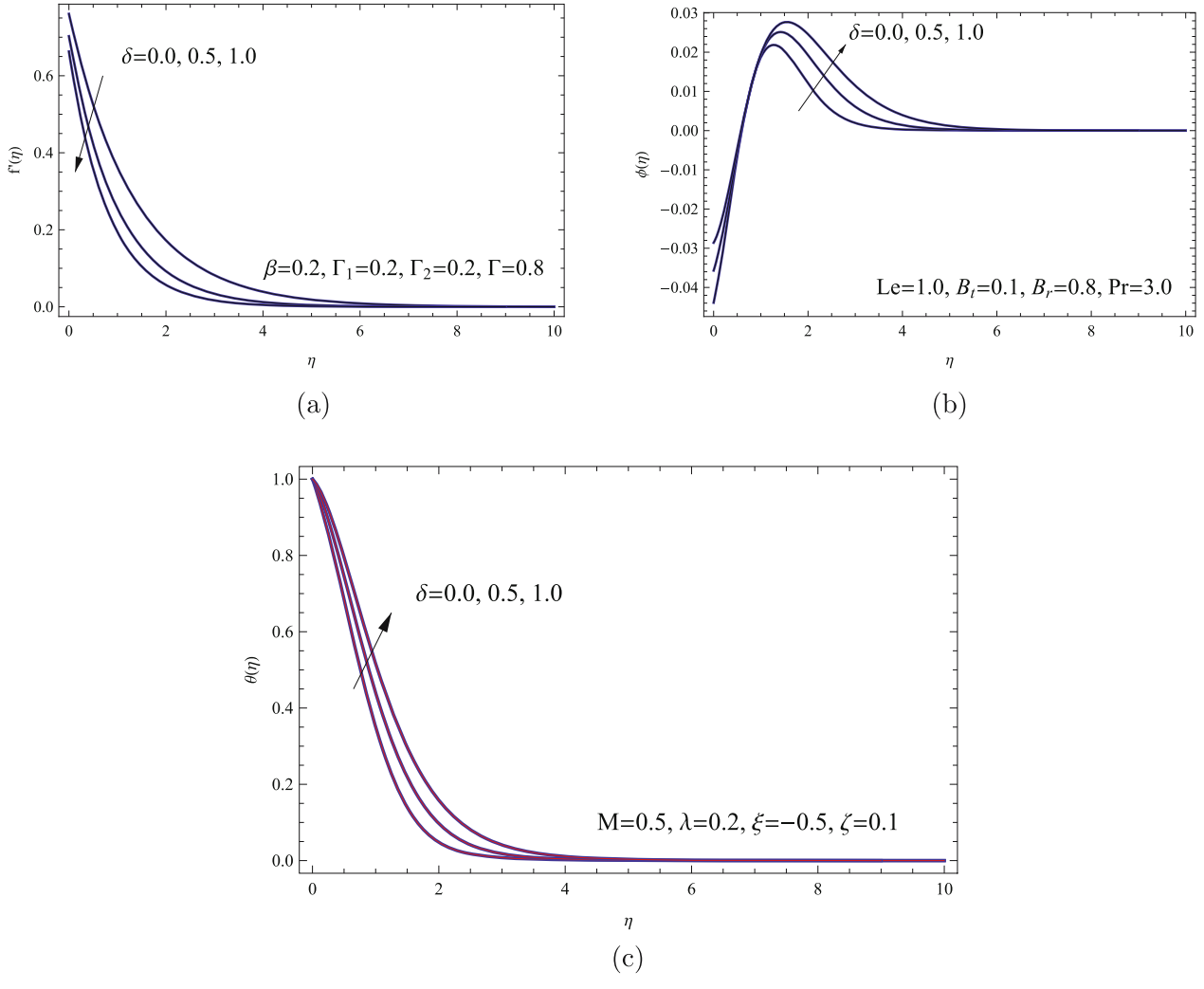

Figure 7: (a) $\theta(\eta)$ and $f'(\eta)$ via varying δ, (b) $\phi(\eta)$ via varying δ, (c) $\theta(\eta)$ via varying δ.

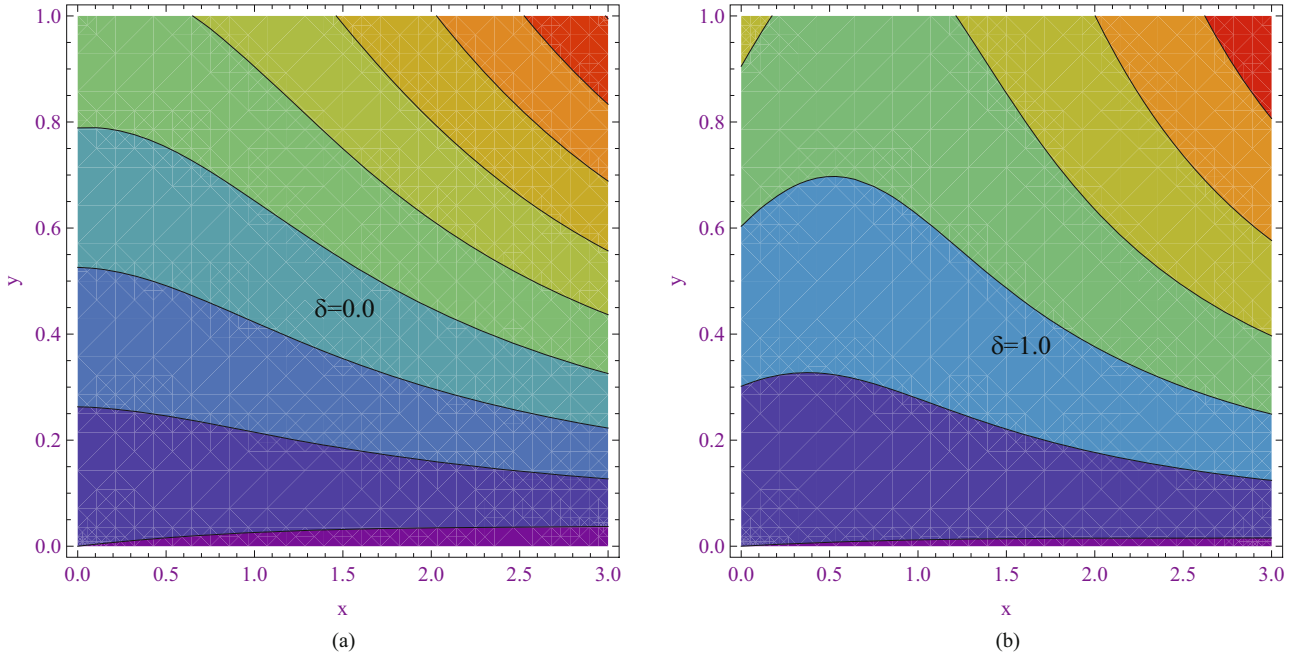

Figure 8: (a) Stream function with δ = 0.0 and (b) stream function with δ = 1.0.

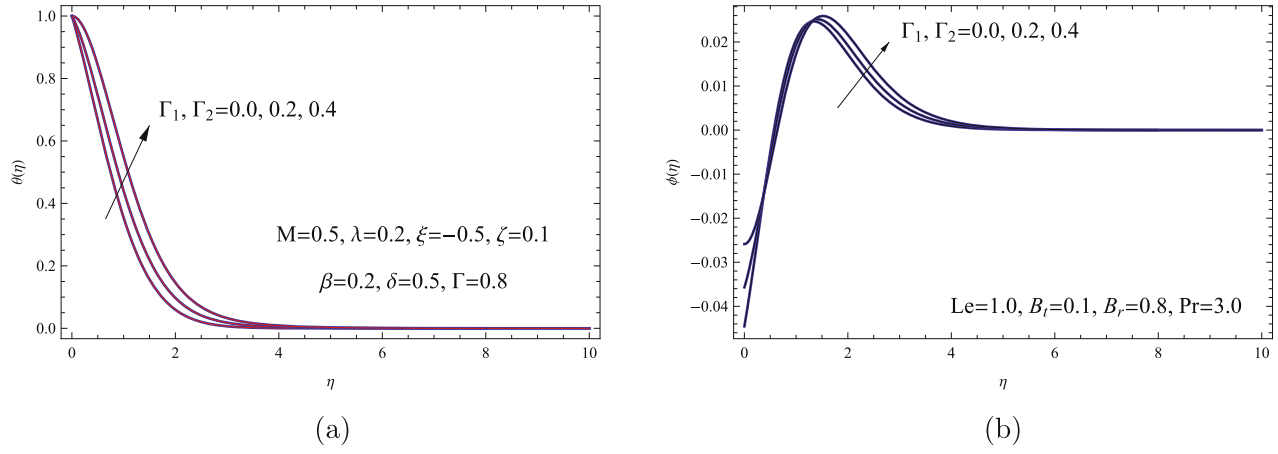

Figure 9: (a) $\theta(\eta)$ via varying Γ_1, Γ_2 and (b) $\phi(\eta)$ via varying Γ_1, Γ_2.

temperature distribution. Further, the practical importance of analyzing magnetic field effects, which are fundamental to a wide range of applications, is explored in greater depth in references [33–35].

In the following graph, the streamlines $\psi(x, y)$ for two distinct cases (M = 0.0, M = 1.0) are examined, as it is clear from Figure 6. Clearly that the Casson nanofluid flow is restricted by the presence of magnetic field, which directly results in decreasing the number of observed streamlines $\psi(x, y)$ compared to the case of absence of a magnetic field, where the fluid flow is more uninhibited and widespread.

Another critical aspect of this work is the investigation of how the porous medium in terms of porous parameter δ impacts the Casson nanofluid behavior. Specifically, we analyzed its effect on velocity $f'(\eta)$, temperature $\theta(\eta)$, and concentration $\phi(\eta)$, as depicted in Figure 7. The fluid concentration exhibits a novel pattern along the elastic sheet: it starting the concentration below zero, it transitions through a zero concentration point, enhances, and then reduces, eventually reaching to zero concentration again but in this case at a point further away the elastic sheet surface. Also, it is essential to examine how the flow within a porous medium can be impacted by the presence of this pores, especially on the fluid's velocity and temperature. Physically, the porous medium, through its intricate network of pores, facilitates a more regulated transfer of thermal energy. However, the

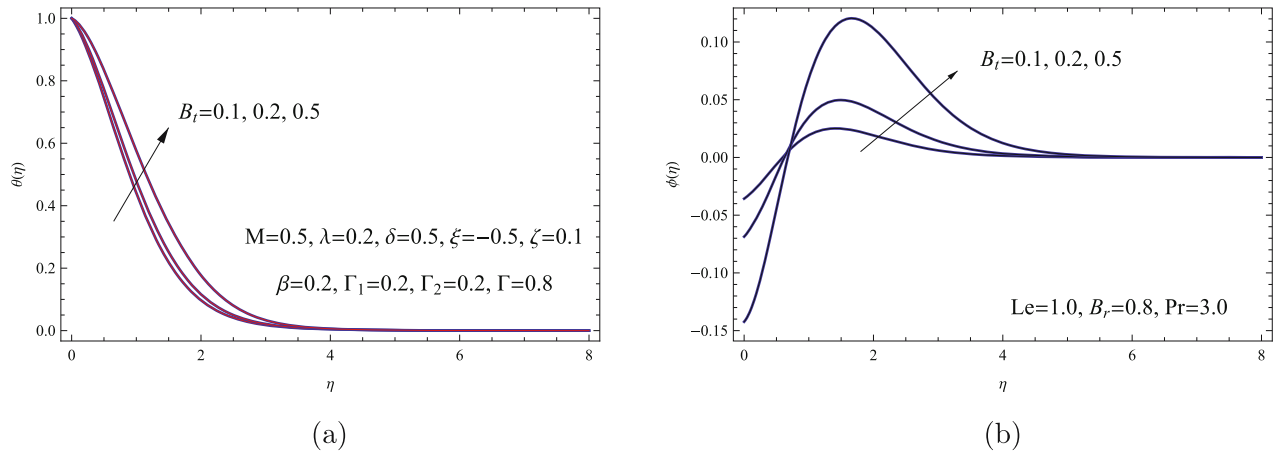

Figure 10: (a) $\theta(\eta)$ via varying B_t and (b) $\phi(\eta)$ via varying B_t.

solid protrusions within the medium introduce additional drag and resistance, which in turn reduce the nanofluid velocity and compress the boundary layer thickness.

Further, to visually compare flow patterns within a momentum boundary layer, streamline curves $\psi(x, y)$ are introduced through Figure 8 for two different cases, porous (δ = 1.0) and nonporous (δ = 0.0) media. As expected, the presence of the pores of the porous medium can create a force in the form of additional resistance, which results in reducing the flow velocity and the corresponding boundary thickness. As a result, a smaller number of streamlines are noted compared to a case in nonporous medium, where the flow becomes greater freedom and has no or fewer restrictions.

The following figure examines the influence of the heat generation parameters Γ_1, Γ_2, one dependent on distance Γ_1 and the other on the temperature difference Γ_2, as shown in Figure 9. It is clear from these curves that both parameters Γ_1, Γ_2 can regulate the temperature distribution $\theta(\eta)$ of the nanofluid as well as enhance this distribution within a limited region ($0.0 \le \eta \le 4.0$) inside the boundary layer. Physically, elevated values of the heat generation parameters Γ_1, Γ_2 intensify internal heating, which amplifies temperature levels, improves thermal diffusion, and causes the thermal boundary layer to grow in thickness. Similarly, these parameters Γ_1, Γ_2 can significantly impact the fluid concentration $\phi(\eta)$ by enhancing it within a specific region ($1.5 \le \eta \le 4.3$) of the boundary layer. After that, the nanofluid concentration collapses until it reaches to zero concentration at a point farther from the sheet surface. Here, it is important to note the crucial role of these parameters in delaying the attainment of zero concentration degree or, in other words, in expanding the region of fluid concentration.

After that, the relationship between the thermophoresis parameter B_t and the resulting temperature $\theta(\eta)$ and concentration $\phi(\eta)$ distributions is visualized in Figure 10. As clearly from the curve, the temperature profile of the Casson nanofluid is significantly controlled by the thermophoresis parameter, which results in a rise behavior in the field of

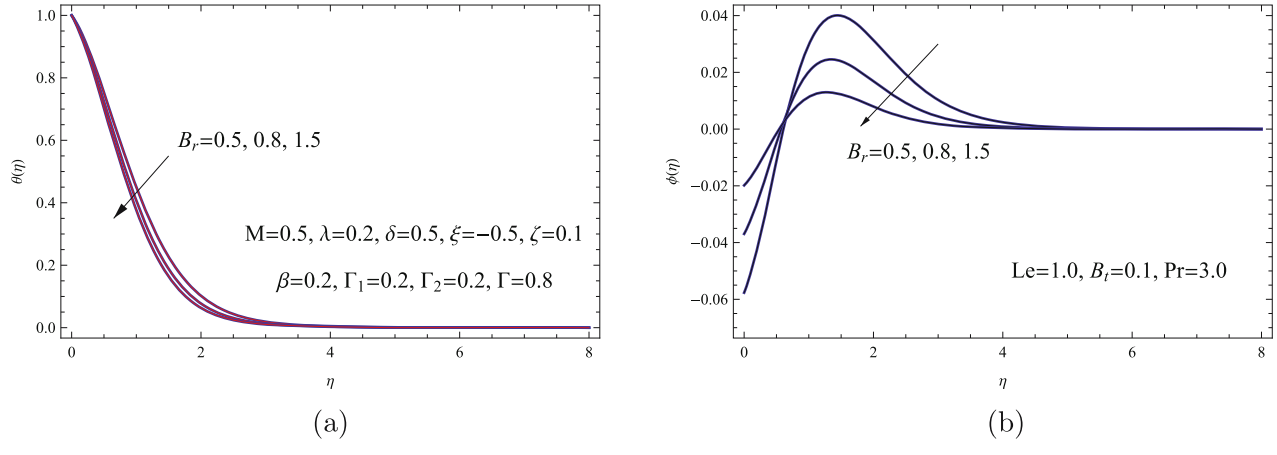

Figure 11: (a) $\theta(\eta)$ via varying B_r and (b) $\phi(\eta)$ via varying B_r.

temperature within a specific region of the boundary layer, especially after η = 1.0, as demonstrated by the curves. Physically, the thermophoretic force, intensified by an increased parameter, propels nanoparticles along thermal gradients from warmer to cooler zones. This phenomenon amplifies thermal energy concentration, facilitates heat redistribution, and leads to a broadening of the thermal diffusion region and a consequent increase in thermal boundary layer thickness. In addition, the same parameter B_t impacts the field of nanofluid concentration by increasing it within a specific region of the boundary layer, away from the sheet surface. However, in close proximity to the surface of elastic sheet, the nanofluid concentration exhibits a notable reversal, experiencing a sharp decline that results in negative concentration values for the Casson nanofluid.

As illustrated in the following curve (Figure 11), the Brownian parameter B_r has a negative effect on the temperature distribution $\theta(\eta)$. This effect is observed within a limited region of the boundary layer ($0 \le \eta \le 3.0$), after which the alteration stabilizes until the temperature reaches zero ($\theta(\eta) \to 0$) at a far distance from the stretching sheet ($\eta \to \infty$). Regarding the fluid concentration $\phi(\eta)$, it shows a notable rise close to the stretching surface ($0 \le \eta \le 0.8$) as Brownian parameter intensifies. But, this trend is not sustained; beyond a certain distance ($\eta \ge 0.8$), heightened Brownian parameter values causes the nanofluid concentration to diminish until reaching to stabilizes at ($\eta \to \infty$). After that, we must turn to the relationship that should not be overlooked through Table 2, which combines between the governing parameters of the physical model and their impact on the surface friction coefficient $\mathrm{Cf}_x\sqrt{\mathrm{Re}_x}$ as well as the heat and mass transfer coefficients $\mathrm{Nu}_x\mathrm{Re}_x^{\frac{-1}{2}}$ and $\mathrm{Sh}_x\mathrm{Re}_x^{\frac{-1}{2}}$. It is clearly evident from the recorded results that the surface friction coefficient increases due to the magnetic number, Brownian motion parameter, porous parameter, and heat generation parameters. However, the effect is reversed negatively due to the slip velocity parameter and the thermophoresis parameter. It is also evident that the relationship between the heat and mass transfer coefficients and the magnetic parameter, porous parameter, and heat generation parameters is an inverse relationship. However, their relationship with the slip velocity parameter is a direct relationship.

6 Concluding remarks

Employing the Thompson–Troian framework, this study analyzes the flow characteristics of a Casson nanofluid, integrating the effects of Stefan blowing, viscous dissipation, nonuniform heat generation, and Cattaneo–Christov thermal flux under slip boundary conditions. Numerical analysis were performed via the shooting method. This study highlight the valuable insights into nanofluid behavior through porous media with magnetic field conditions. Based on the entire study conducted. the following key findings were made as follows:

1) Elevating the slip parameter diminishes skin friction by 48% and augments mass transfer by 8%. Conversely, intensifying the magnetic field increases skin friction by 25% while inhibiting heat transfer by 52%.
2) Brownian, magnetic, porous, and heat generation factors raise friction, while slip and thermophoresis factors lower it.
3) Less number of streamlines are observed in the porous medium and the case of presence of magnetic field, whereas the nonporous medium or the absence of magnetic field allows freer flow with minimum restrictions that create more streamlines.
4) Heat and mass transfer rates inversely relates to magnetic, porous, heat generation factors; but directly to slip.
5) Porous parameter slows flow motion, shrinks the boundary layer thickness, and reduces streamlines compared to unrestricted flow with porous medium.
6) At a distance from a sheet surface, nanofluid concentration drops to zero; magnetic field affects Casson nanofluid's speed and its corresponding heat.

Funding information: The author states no funding involved.

Author contributions: The author confirms the sole responsibility for the conception of the study, presented results and manuscript preparation.

Conflict of interest: The author states no conflict of interest.

Data availability statement: All data generated or analysed during this study are included in this published article.

References

[1] Choi SUS. Enhancing thermal conductivity of fluid with nanoparticles, developments and applications of non-Newtonian flow. ASME FED. 1995;231:99–105.
[2] Noor NAM, Shafie S, Admon MA. Slip effects on MHD squeezing flow of Jeffrey nanofluid in horizontal channel with chemical reaction. Mathematics. 2021;9:1215.

[3] Al Rashdi SA, Ghoneim NI, Amer AM, Megahed AM. Investigation of magnetohydrodynamic slip flow for Maxwell nanofluid over a vertical surface with Cattaneo-Christov heat flux in a saturated porous medium. Results Eng. 2023;19:101293.
[4] Sankari MS, Rao EM, Khan W, Alshehri MH, Eldin SM, Iqbal S. Analytical analysis of the double stratification on Casson nanofluid over an exponential stretching sheet. Case Stud Therm Eng. 2023;50:103492.
[5] Ilango MS, Lakshminarayana P. Effects of double diffusion and induced magnetic field on convective flow of a Casson nanofluid over a stretching surface. Heliyon. 2024;10:e31040.
[6] Reddy MV, Vajravelu K, Ajithkumar M, Sucharitha G, Lakshminarayana P. Numerical treatment of entropy generation in convective MHD Williamson nanofluid flow with Cattaneo-Christov heat flux and suction/injection. Int J Model Simulat. 2024;1–18. doi: https://doi.org/10.1080/02286203.2024.2405714.
[7] Goher S, Abbas Z, Rafiq MY. Shear flow of two immiscible non-Newtonian nanofluids considering motion of motile microorganisms. Int J Thermofluids. 2025;27:101282.
[8] Abbas Z, Rafiq MY, Fayyaz A. Peristaltic flow of carbon nanotube-based hybrid nanofluid in the annular region of eccentric cylinders with a modified thermal conductivity model. Multiscale Multidiscip Model Exp Des. 2025;8:250.
[9] Navier CLMH. Sur les lois du mouvement des fluides. Mem Acad R Sci Inst Fr. 1827;6:389–440.
[10] Maxwell JC. On stresses in rarified gases arising from inequalities in temperature. In: The scientific papers of James Clerk Maxwell. Niven WD, editors. Vol II. Cambridge: Cambridge University Press; 1890. p. 681–712.
[11] Thompson PA, Troian SM. A general boundary condition for liquid flow at solid surfaces. Nature. 1997;389:360–2.
[12] Ahmad S, Nadeem S. Flow analysis by Cattaneo-Christov heat flux in the presence of Thompson and Troian slip condition. Appl Nanosci. 2020;10:1–15.
[13] Nadeem S, Ahmad S, Khan MN. Mixed convection flow of hybrid nanoparticle along a Riga surface with Thompson and Troian slip condition. J Therm Anal Calorimetry. 2021;143:2099–109.
[14] Gangadhar K, Seshakumari PM, Rao MVS, Chamkha AJ. MHD flow analysis of a Williamson nanofluid due to Thompson and Troian slip condition. Int J Appl Comput Math. 2022;8:6.
[15] Dey S, Mukhopadhyay S, Mandal MS. Influence of Thompson and Troian slip on the nanofluid flow past a permeable plate in porous medium. Pramana J Phys. 2023;97:66.
[16] Alrehili M. Stagnation flow of a nanofluid with rough surface and energy dissipation: A tangent hyperbolic model with practical engineering uses. Results Eng. 2025;26:104825.
[17] Fang T, Jing W. Flow, heat and species transfer over a stretching plate considering coupled Stefan blowing effect from species transfer. Commun Non-linear Sci Numer Simul. 2014;9:3086–97.
[18] Konai S, Maiti H, Mukhopadhyay S. Influences of Stefan blowing on unsteady flow of Casson nanofluid past a stretching surface. Forces Mechanics. 2023;12:100227.
[19] Saleem M, Hussain M. Impression of nonlinear radiation and Stefan blowing on the magneto cross nano-Williamson fluid above exponentially stretching sheet. Results Eng. 2023;17:100864.
[20] Dey S, Mukhopadhyay S. Stefan flow of nano liquid passing a plate surface with changeable fluid properties. Partial Differ Equ Appl Math. 2024;9:100632.
[21] Challa KK, Rao ME, Jawad M, Saidani T, Abdallah SAO, Thenmozhi D. Enhanced heat transfer and flow dynamics of Powell-Eyring nanofluid: unsteady stretched surface and with Stefan blowing/suction. Case Studies Thermal Eng. 2025;65:105664.
[22] Khan SU, Tlili I, Waqas H, Imran M. Effects of nonlinear thermal radiation and activation energy on modified second-grade nanofluid with Cattaneo-Christov expressions. J Therm Anal Calorim. 2021;143:1175–86.
[23] Abbas W, Megahed AM, Morsy OM, Ibrahim MA, Ahmed AM. Said dissipative Williamson fluid flow with double diffusive Cattaneo-Christov model due to a slippery stretching sheet embedded in a porous medium. AIMS Math. 2022;7:20781–96.
[24] Alrehili M. Exploring Sutterby fluid flow over a stretched surface in porous media with non-Newtonian dissipation and Cattaneo-Christov heat/mass flux models. Canad J Phys. 2025;103:901–11.
[25] Khader MM, Megahed AM, Eid A. Numerical treatment of the radiated and dissipative power-law nanofluid flow past a nonlinear stretched sheet with non-uniform heat generation. Sci Rep. 2023;13:22691.
[26] Alali E, Megahed AM. MHD dissipative Casson nanofluid liquid film flow due to an unsteady stretching sheet with radiation influence and slip velocity phenomenon. Nanotech Rev. 2022;11:463–72.
[27] Rafiq MY, Mustafa G, Abbas Z. Dynamics of the ohmic heating and chemically reactive time-dependent flow of magnetized Casson fluid inside a rectangular pipe. Numer Heat Transfer Part A Appl. 2024;1–24. doi: https://doi.org/10.1080/10407782.2024.2361468.
[28] Abbas Z, Rafiq MY, Asghar H, Khaliq S. Exploration of the dynamics of non-Newtonian Casson fluid subject to viscous dissipation and Joule heating between parallel walls due to buoyancy forces and pressure. Proc IMechE Part E J Process Mech Eng. 2024;238:912–21.
[29] Abbas Z, Sheikh M, Hasnain J, Ayaz H, Nadeem A. Numerical aspects of Thompson and Troian boundary condition in Tiwari Dasnanofluid model with homogeneous-heterogeneous reactions. Phys Scr. 2019;94:11.
[30] Zhang R, Zaydan M, Alshehri M, Raju CSK, Wakif A, Shah NA. Further insights into mixed convective boundary layer flows of internally heated Jeffery nanofluids: stefan's blowing case study with convective heating and thermal radiation impressions. Case Stud Therm Eng. 2024;55:104121.
[31] Amer AM, Al Rashdi SAS, Ghoneim NI, Megahed AM. Tangent hyperbolic nanofluid flowing over a stretching sheet through a porous medium with the inclusion of magnetohydrodynamic and slip impact. Results Eng. 2023;19:101370.
[32] Akbar NS, Ebaid A, Khan ZH. Numerical analysis of magnetic field effects on Eyring-Powell fluid flow towards a stretching sheet. J Magn Magn Mater. 2015;382:355–8.
[33] Meenakumari R, Lakshminarayana P, Vajravelu K. Influence of induced magnetic field and slip conditions on convective Prandtl fluid flow over a stretching surface with homogeneous and heterogeneous reactions. Multidiscip Model Materials Struct. 2020;24:127–47.
[34] Mujahid M, Abbas Z, Rafiq MY. A study on the pressure-driven flow of magnetized non-Newtonian Casson fluid between two corrugated curved walls of an arbitrary phase difference. Heat Transfer. 2024;53:4510–27.
[35] Meenakumari R, Rani PY, Sucharitha G, Vajravelu K, Lakshminarayana P. Thermal inspection on MHD Prandtl fluid flow past a stretching sheet in the presence of heat generation/absorption and suction/injection. Phys Scr. 2025;100:025237.